DESIGN AND PERFORMANCE OF A FISH FIN-LIKE PROPULSOR FOR AUVS

George V. Lauder[1], Peter Madden[1], Ian Hunter[2], James Tangorra[2], Naomi Davidson[2], Laura Proctor[2], Rajat Mittal[3], Haibo Dong[3], and Meliha Bozkurttas[3]

[1]Department of Organismic and Evolutionary Biology, Harvard University, 26 Oxford St., Cambridge, MA 02138, Phone: 617-496-7199; Email: Glauder@oeb.harvard.edu

[2] BioInstrumentation Laboratory, Massachusetts Institute of Technology, Room 3-147, 77 Massachusetts Ave., Cambridge, MA 02139

[3]Department of Mechanical and Aerospace Engineering, 707 22nd Street, Staughton Hall The George Washington University, Washington, D.C.

***Abstract* -- Fishes are noted for their ability to maneuver and to position themselves accurately even in turbulent flows. This ability is the result of the coordinated movement of fins which extend from the body and form multidirectional control surfaces that allow thrust vectoring. We have embarked on a research program designed to develop a maneuvering propulsor for AUVs based on the mechanical design and performance of fish fins. To accomplish this goal, we have taken a five-pronged approach to the analysis and design of a propulsor based on principles derived from the study of fish fin function. First, we have undertaken a detailed investigation of 3D kinematic patterns exhibited by fish fins during locomotion. Second, we have measured the mechanical properties of fish fin rays and membrane that comprise the propulsive surface. Third, we have studied the hydrodynamics of fish fin function using digital particle image velocimetry (DPIV) on the fins of freely swimming fishes. Fourth, a computational fluid dynamic (CFD) study of fish fin function has been produced that allows calculation of fin flow patterns using actual 3D fish fin kinematics and allowing bending and fin area changes during the fin stroke. Fifth, a first generation biomimetic, physical, robotic model of the bluegill sunfish pectoral fin has been developed that can reproduce the complex fin motions that fishes use for propulsion and maneuvering.**

Fish fins are remarkable propulsive devices and can serve as inspiration for designing the next generation of AUV control surfaces.

I. INTRODUCTION

Fishes are remarkable in their ability to maneuver and accurately control body position even in turbulent flows. In addition, many fishes can spin on their long axis using only individual pairs of fins such as the pectoral fins. This ability is the result of the coordinated movement of fins which extend from the body and form multidirectional control surfaces that allow thrust vectoring. We have embarked on a research program designed to develop a maneuvering propulsor for AUVs based on the mechanical design and performance of fish fins.

II. THE SUNFISH MODEL SYSTEM

Bluegill sunfish (*Lepomis macrochirus*) are highly maneuverable bony fishes which have been the subject of a number of previous experimental analyses of locomotor function (*1-6*) and serve as excellent experimental subjects for an integrated approach to understanding the function of fish fins, deriving the principles of fish fin function, and applying these principles to construction of a biomimetic robotic fin for use in maneuvering AUVs.

Sunfish are able to execute highly effective yaw maneuvers using only their pectoral fins, and at speeds of less than 1.1 body length per second use only their pectoral fins for propulsion.

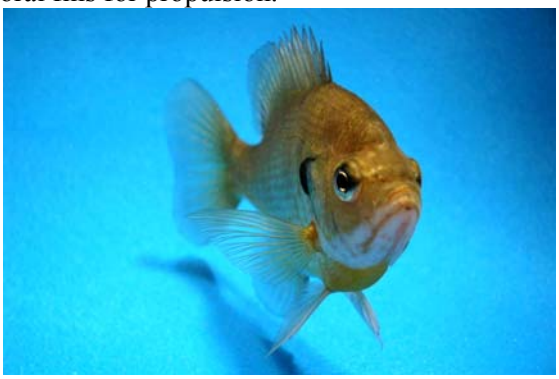

Figure 1. Bluegill sunfish showing the right pectoral fin extended from the body.

Sunfish pectoral fins are also representative of the structure of the vast majority of bony fish fins (*7-9*) in possessing bony fin rays joined by a thin collagenous membrane.

III. 3D FIN KINEMATICS

Motion of the sunfish pectoral fin during both propulsion and maneuvering was quantified using two calibrated high-speed video cameras recording simultaneously at 250 and 500 fps with 1024 *1024 pixel resolution. Digitizing up to 300 points per time step in 3D, and using approximately 20 time increments per fin beat allowed detailed reconstruction of 3D fin motion.

Pectoral fin motion in three dimensions is very complex (Figs. 1 and 2) and involves (1) simultaneous movement of the upper and lower fin edges away from the body, forming *two simultaneous leading edges*, (2) strong cupping of the fin as it moves away from the body, (3) a wave of bending that moves spanwise along the upper edge of the fin at higher than free-stream flow velocity, (4) "dimpling" of the upper fin surface behind the leading edge (also see Fig. 13), (5) substantial reorientation of the fin base and rotation of the fin (Figs. 2, 3), and (6) significant area changes during the fin beat (Fig. 4).

During maneuvering, substantial changes in fin orientation throughout the fin beat occur as the fin rotates dramatically around its spanwise long axis (Fig. 3) to generate the side forces needed to rotate the fish body in yaw.

Fin flexibility and dramatic shape change are hallmarks of fish propulsion and maneuvering, and distinguish fish fins from human engineered and bird and insect propulsion systems.

Figure 1. Portion of a frame from high-speed video of bluegill sunfish swimming at 1.0 Ls^{-1}. Note the wave of bending that travels out along the fin upper edge and the high degree of fin flexibility.

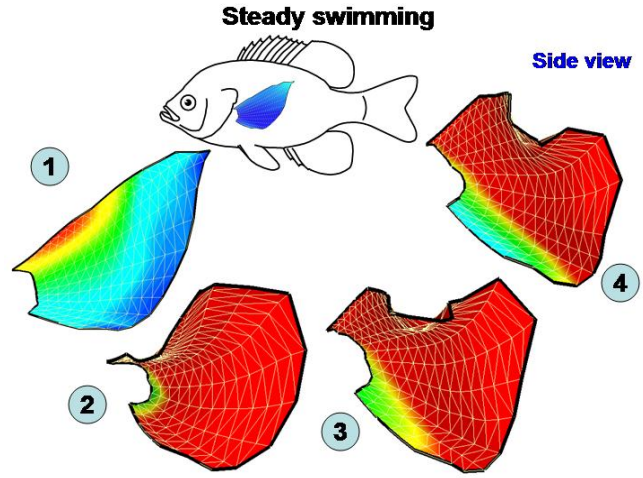

Figure 2. Conformations of the sunfish pectoral fin at four times during the fin beat during steady locomotion. Color reflects distance from the body, with blue indicating positions near the body, and red positions away from the body.

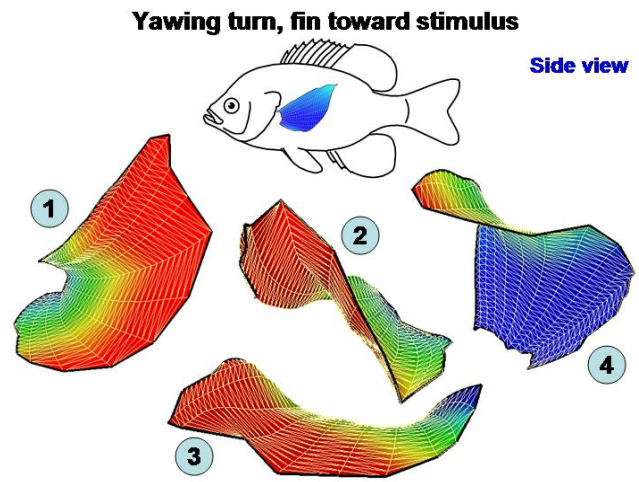

Figure 3. Conformations of the sunfish pectoral fin at four times during the fin beat during a yawing turn. Color code as in Fig. 2 above.

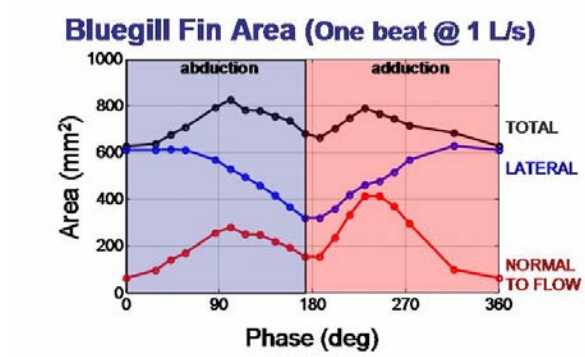

Figure 4. Changes in pectoral fin area during one steady swimming beat.

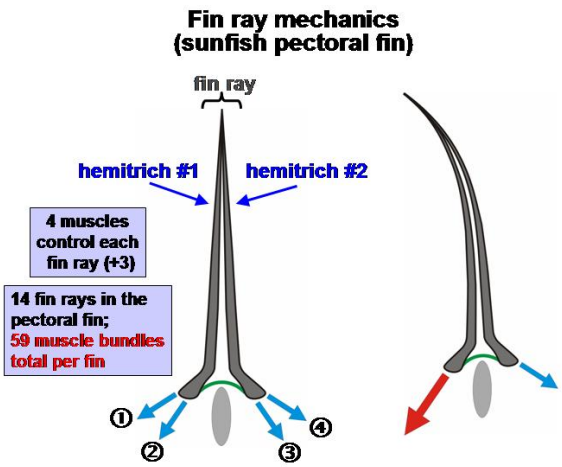

Figure 5. Schematic cross-section of a fin ray to show the bilaminar design of fin rays in bony fishes.

IV. FIN MECHANICAL PROPERTIES

The fin rays of fishes and the membrane that spans between adjacent rays possess a remarkable functional design that allows active control of the fin surface by musculature at the base of the fin. Figure 5 shows the basic design of a fin ray. Each ray possesses two halves (hemitrichs) attached to each other along their length by collagen and elastic fibers. Each half ray also receives numerous muscle attachments that allow the fish to actively control ray bending by displacing one ray relative to the other (Fig. 5). Three-point bending tests (Fig. 6) show that different fin rays in the fin vary in stiffness both along their length and among rays (Fig. 7).

By removing individual fin rays and clamping each half ray to actuators, we were able to make additional measurements of (1) force input to the half rays versus force output near the tip of the fin, and (2) displacement input at the fin ray base versus tip displacement.

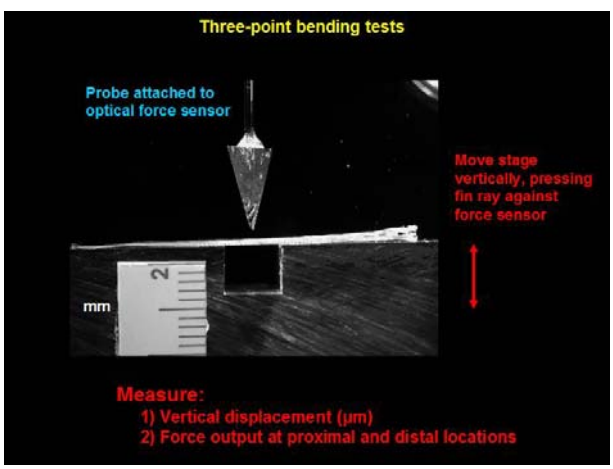

Figure 6. Three point bending of a sunfish fin ray. Force is measured by the probe above.

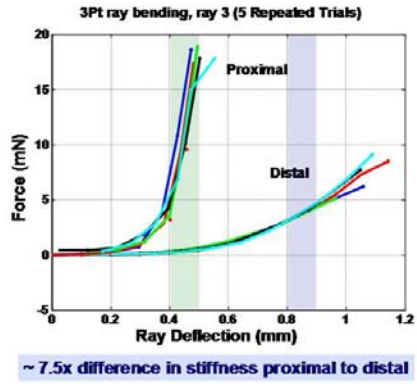

Figure 7. Sunfish fin ray stiffness varies nearly 8-fold along the ray.

Flexural stiffness = E*I
(x 10^{-6} Nm^2)

	proximal	distal
Ray 1	0.3	
Ray 2	1.4	0.1
Ray 6	3.2	0.1
Ray 8	0.8	0.05
Ray 12	0.05	

Flexural stiffness changes 14 – 32x along rays

Figure 8. Flexural stiffness of sunfish fin rays at two locations along the ray.

Fin ray "Composite" Young's Modulus (E)
(GPa)

	proximal	distal
Ray 1	3.4	
Ray 2	1.5	0.4
Ray 6	1.2	0.1
Ray 8	0.6	0.1
Ray 12	0.2	

E within rays varies 3 – 12x

Some comparative data for E:
- **Bovine femur: ~ 20 GPa**
- **Human tendon: ~ 0.5 GPa**
- **Delrin plastic: ~ 2.6 GPa**

Figure 9. Young's Modulus of fish fin rays calculated for two locations along the ray..

Calculated stiffness of rays at two locations (Fig. 7) shows that stiffness can vary up to 7.5 fold along rays. Stiffness also varies among fin rays and the rays in the middle of the fin appear to be the stiffest. Flexural stiffness (E*I) varies up to 32-fold among fin rays within the pectoral fin (Fig. 8).

Young's Modulus of the whole "composite" ray also varies considerably but is on the order of values for human tendon: 1 GPa (Fig. 9).

Measurements of force input and output of fin rays reveal that there is a 30:1 ratio reflecting the primary role of the fin rays as displacement transducers: force transmission is relatively inefficient.

Fin ray curvature varies by a factor of 3 among rays. For example, applying 20mN of force to the base of a ray can generate from 0.1 to 0.33 mm^{-1} curvature.

Uniaxial tensile tests were also performed on the pectoral fin webbing of bluegill sunfish in order to determine its stress-strain characteristics. As shown in Figure 10, samples of the fin webbing, approximately 1 to 3 mm in length and 500 to 900 µm in width, were cut from sunfish fins. Length was measured perpendicular to the fin rays. The fin rays were left attached to the webbing so that the webbing specimen could be grasped easily by two clamps at the fin rays. Engineering stress and strain were calculated from measurements of force and the specimen's length, width, and thickness.

Representative results from two specimens are shown in Figure 11. The slope of the graphs represents the webbing's modulus of elasticity. In each of the graphs several large changes in the slope, referred to as knees of the graph, can be seen to occur at similar stress magnitudes. These knees are likely due to fibers fracturing. Under the first knee, which is at 10 kPa, the modulus of elasticity is approximately constant at 250 $\times 10^3$ N/m^2 for Test 1 and 150 $\times 10^3$ N/m^2 for Test 2. Between the first and the second knee, which occurs between 75 and 80 kPa, the modulus increases to between 400 and 500 $\times 10^3$ N/m^2. The region from 80 kPa to 130 kPa contains the largest modulus values which exceed 1.3×10^6 N/m^2 for both tests. The final region before the stress values decay has an average modulus of 930×10^3 N/m^2 for Test 1 and 1100 $\times 10^3$ N/m^2 for Test 2. The drop in stress after the peak in the stress-strain curves is due largely to the tearing of the webbing. It is clear from this stress-strain analysis that the fin webbing does not behave like a linear elastic material. The nonlinear stress-strain relationship where the modulus increases throughout the curve until just before the peak is commonly seen in bioviscoelastic solids. The "toe" of the graph, which is defined as the region under the first knee, is indicative of the range of stresses experienced by a biomaterial in normal use. Fracturing fibers is not typical in the normal range of movement, thus the first knee in the graph is a good indicator of the range of stresses the fin webbing will undergo.

The design of the fish fin propulsive surface with active control over surface curvature allows fish actively to resist hydrodynamic loading on the fin, and represents a fundamentally different propulsive design from the feathers and wings that characterize bird and insect locomotor systems respectively.

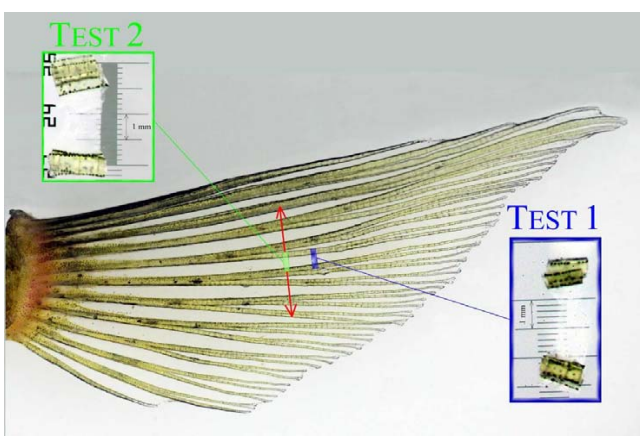

Figure 10. Left pectoral fin used in tensile testing of webbing material. The rectangles overlaid upon the fin indicate the locations for tests one and two. The arrows indicate the direction of force for the tensile tests. The two sample bits are seen in the boxes. Part of the fin ray is left on the webbing bits to ease in grasping during testing.

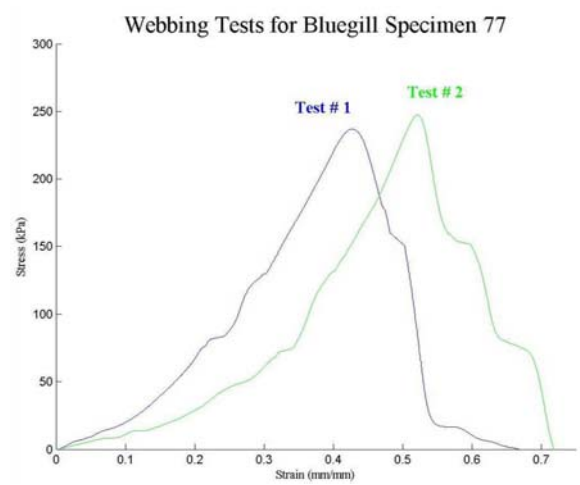

Figure 11. Stress-strain results for bluegill pectoral fin webbing.

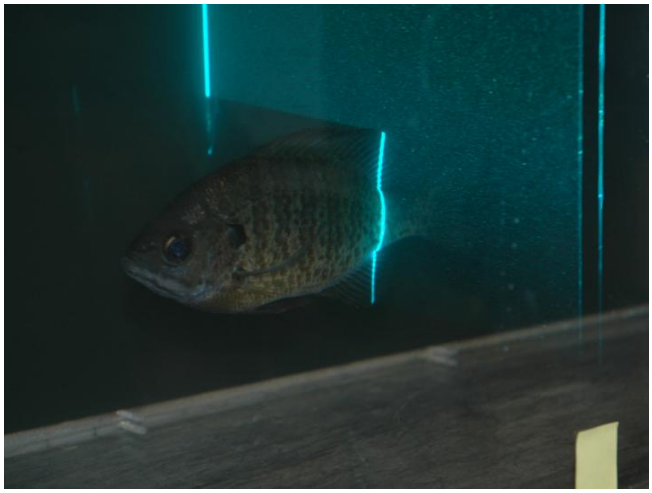

Figure 12. Photograph of a bluegill sunfish swimming in a flow tank intersecting a light sheet used to quantify pectoral fin flow in the transverse plane.

V. EXPERIMENTAL FIN HYDRODYNAMICS

Past experimental hydrodynamic data on fish fins has demonstrated clearly that fins shed vortex rings and that these vortex rings reflect momentum added to the water by beating pectoral fins (*2, 4, 10*). But this experimental hydrodynamic research has been limited by low vector density resulting from relatively low resolution cameras, and a focus on 2D horizontal and vertical slices of the wake behind the fin.

In this study of pectoral fin hydrodynamic function, we have utilized a transverse light sheet (Fig. 12)

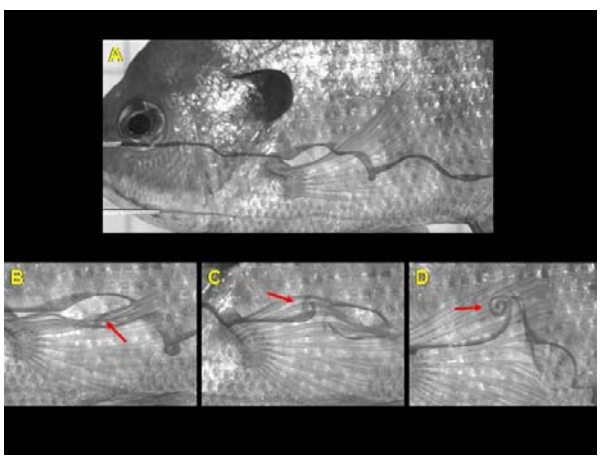

Figure 13. Frames from high-speed videos of dye flow patterns around the sunfish pectoral fin. In panel A the left pectoral fin is about to intercept the dye steam on the downstroke. Red arrows in panels B, C, and D respectively point to dye that is located in the upper edge "dimple", entrained there from the upper edge vortex, dye in the upper edge vortex at the mid-fin position, and dye in a tight upper edge vortex at the distal 1/3 fin position.

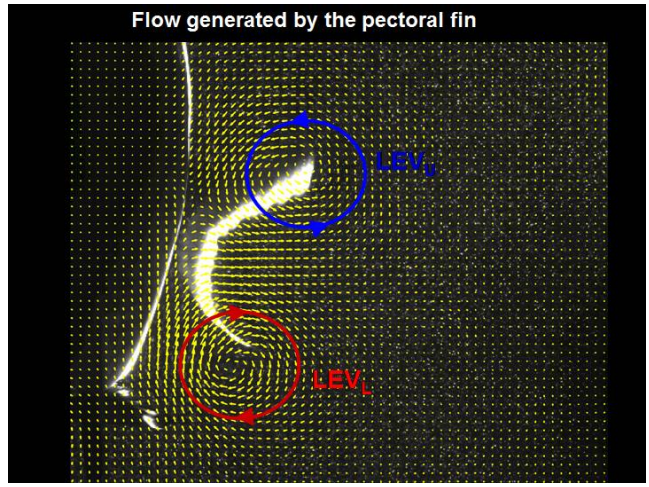

Figure 14. DPIV data from the transverse plane (view from behind the fish, with the cupped pectoral fin moving away from the body in the "downstroke" to the right in this view) showing the two large simultaneous leading edge vortices , LEV, LEV$_U$ and LEV$_L$ on the upper and lower leading edges of the cupped fin.

which provides a complete transect of flow in the wake. By using two simultaneous high-resolution (1024 * 1024 pixel) high speed video cameras operating at 500 fps, we were able to obtain stereo-dpiv data to simultaneously measure u, v, and w flow components within the light sheet. Because we sampled the transverse light sheet at 500 fps, we are then able to reconstruct the time course of flow and estimate three-dimensional wake structure (see the preliminary visualization presented in Figure 16). This light sheet orientation also makes it possible to image flow over the fin surface and between the fin and the body (e.g., Fig. 14).

To compliment the dpiv analyses, we conducted a series of experiments in which fish were induced to swim through dye streams that were directed at the leading edges of the pectoral fin. These data (Fig. 13) show that dye is entrained into the upper leading edge vortex (LEV) which spirals over the upper fin edge and then out spanwise along the fin. Dye spiraling along the upper LEV can be seen trapped in the "dimple" behind the upper leading edge (Fig. 13B). The distinct vortex formed by the upper fin edge (Fig. 13C, D) is visible as the fin adducts and moves toward the body wall.

DPIV data from the transverse light sheet during steady propulsion (Fig. 14) demonstrates two simultaneous leading edge vortices as the fin moves away from the body. The cupped conformation of the pectoral fin at this time is clearly visible and the active side movement of both the upper and lower fin edges produces a distinct pair of attached vortices on the fin.

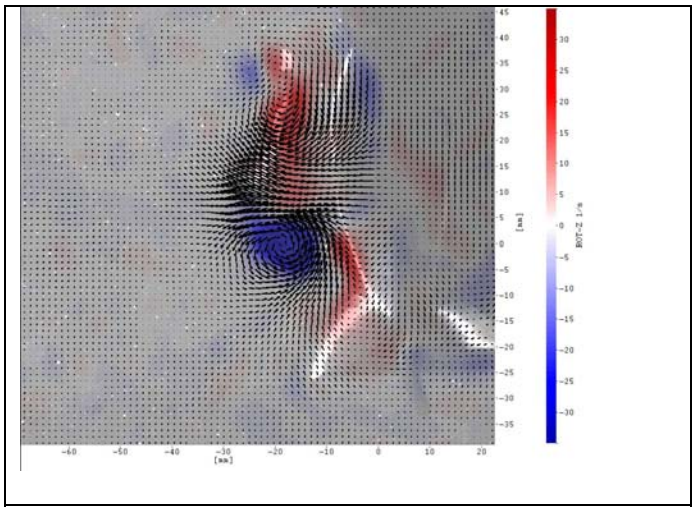

Figure 15. Posterior view of sunfish (pectoral fin is on the left side) at the beginning of a downward maneuver. Note that the lower leading edge of the pectoral fin has moved away from the body in advance of the upper leading edge to generate stronger vorticity. Blue and red colors denote counterclockwise and clockwise vorticity respectively. The fin is moving out to the left in this view, away from the body.

During maneuvering, the lower leading edge of the pectoral fin can move away from the body prior to the upper leading edge to generate much stronger vorticity early in the fin beat than the upper edge (Fig. 15). This is typically seen during downward maneuvers when the fin moves to cause the center of mass to move toward the bottom of the flow tank.

Visualization of flow resulting from pectoral fin movement (Fig. 16) shows a complex pattern of vortical structures similar in character to that resulting from CFD calculations of fin flow (see below). Ongoing research will investigate these wake flow patterns in more detail and quantify momentum added in the free-stream for comparison to results from CFD analyses.

The overall picture that emerges from experimental hydrodynamic analyses of freely-swimming sunfish is that fin flexibility, especially independent control of the upper and lower fin edges, is critical to both propulsion via the generation of two simultaneous LEVs, and maneuvering, during which the lower and upper fin edges can move independently to direct fluid flow.

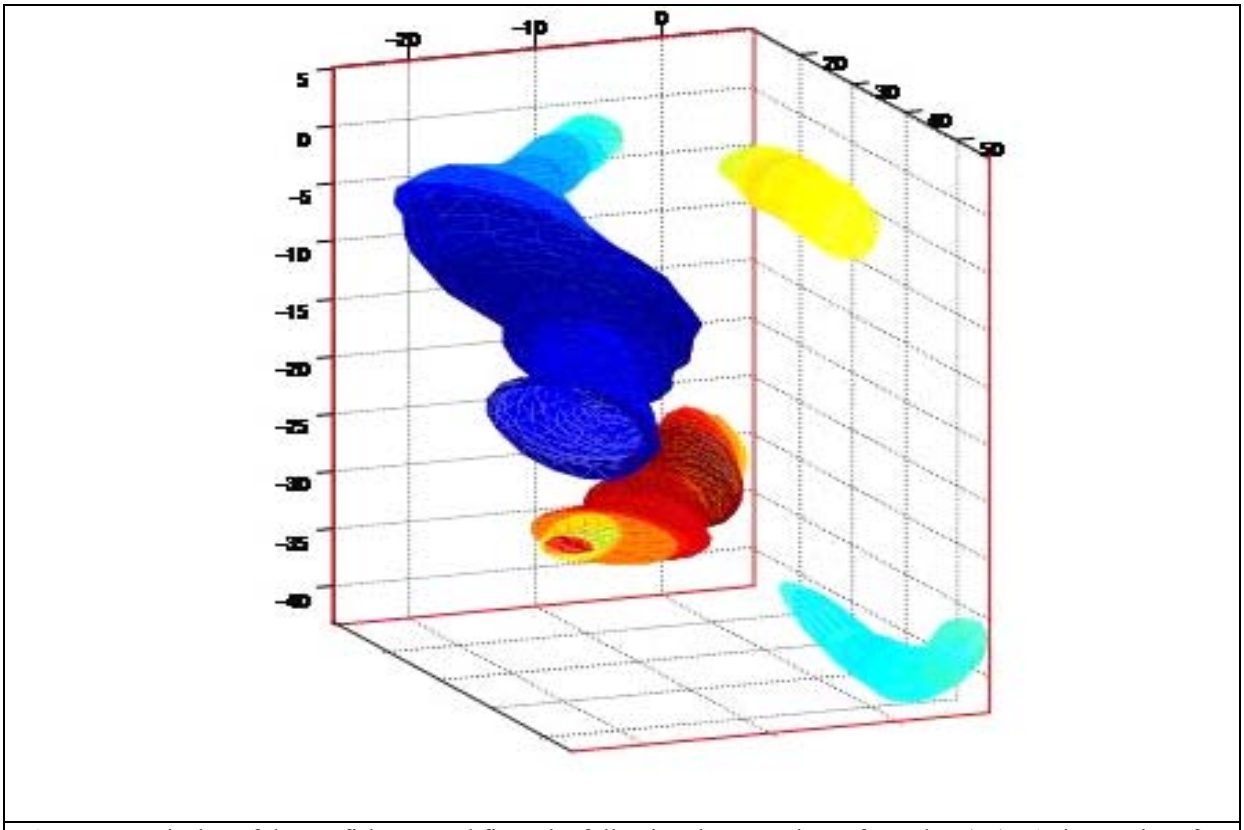

Figure 16. Display of the sunfish pectoral fin wake following the procedure of Brucker (*11*). A time series of transverse PIV slices have been assembled into a three-dimensional depiction of the fin wake. Isosurface contours represent positive (red/yellow) and negative (blue) vorticity in the wake of the pectoral fin. The dark blue and red cones reflect vorticity shed from the leading and trailing edges of the pectoral fin during abduction (movement away from the body), while the yellow and light blue cones represent vorticity shed from the fin edges on the upstroke back toward the body.

VI. COMPUTATIONAL MODELING

High-fidelity numerical simulations are being used to examine the key hydrodynamic features and thrust performance of the bluegill sunfish pectoral fin. The computer modeling approach employs a recently developed parallelized immersed boundary solver (*12, 13*) which can perform direct (DNS) or large-eddy simulation (LES) of flow past highly deformable bodies such as the fish pectoral fin. The code has been extensively validated and runs quite efficiently on very large (500+ CPUs) multi-processor computers. The CFD effort is closely tied to the experimental work being done on fin hydrodynamics and complements this work by providing data and analyses that are not available from the experiments.

CFD Analysis of Fin Hydrodynamics

The CFD objective is to examine the flow past a pectoral fin of a bluegill sunfish which is in steady forward motion and to quantify the thrust performance of this fin using the actual 3D fin kinematics described above. Figure 17 shows the side view of the vortex structures for the pectoral fin at three different times during the cycle. In this figure, *x*-and z- are the streamwise and spanwise directions respectively. The body of the fish is shown for viewing purpose only and is not included in the simulations. A $152 \times 132 \times 96$ Cartesian grid is used in the current simulations. The Strouhal number is 0.54 and matches that in the experiment. The Reynolds number of the simulations is four times lower than that in data obtained from live sunfishes. Simulations at the experimental Reynolds are currently being carried out on a larger mesh. Strouhal number is 0.54 and matches that of the experiment. The Reynolds number four lower than that in the experiment. Simulations at the experimental Reynolds are currently being carried out on a larger mesh.

The figure shows a very complex system of vortices being generated by the fin as it moves through a complete cycle. Of particular note is the strong tip vortex observed in Figure 1(c) as well as leading edge vortices created by the top edge of the fin both during abduction and adduction. PIV measurements taken of the flow past the fish pectoral fin in steady swimming are used to validate the current simulations. It should be noted that the fish fin kinematics which are employed in the CFD are not measured simultaneously with the PIV measurements. This introduces some degree of variability between the CFD simulations and the PIV experiments. Nevertheless, we expect the numerical simulations to match most of the key topological features of the flow. Figure 18 shows a set of three plots comparing flow velocity vectors between CFD and PIV at a streamwise plane shown in Figure 1(c) which is located roughly 2/3 L downstream from the fin root. Figure 18(a) corresponds to an early time in the cycle where the fin is initiating its motion away from the body and is simultaneously undergoing a "cupping" motion that rapidly accelerates its upper and lower fin tips.

A consequence of this rapid acceleration is the formation of two tip vortices where the upper (dorsal) vortex is stronger than the lower (ventral) one. It is clear that both PIV and CFD show these distinct features. Figure 18(b) is roughly at the 1/3 stage in the cycle. Despite some mismatch between the two fin shapes at this time instant, we find that the CFD and PIV continue to show the presence of two tip vortices. Finally, Figure 18(c) shows a time instant where the cycle is almost complete and the fin moving towards the body. At this time instant, the PIV measurements show only one vortex which is attached to the upper tip and the CFD simulations also reproduce a similar behavior. Thus overall, the comparison between the experiments and CFD is quite reasonable and confirms the fidelity of the numerical simulations. It should be pointed out that this is the first time that such detailed comparisons between flow measured past a swimming animal and corresponding CFD generated data have been made.

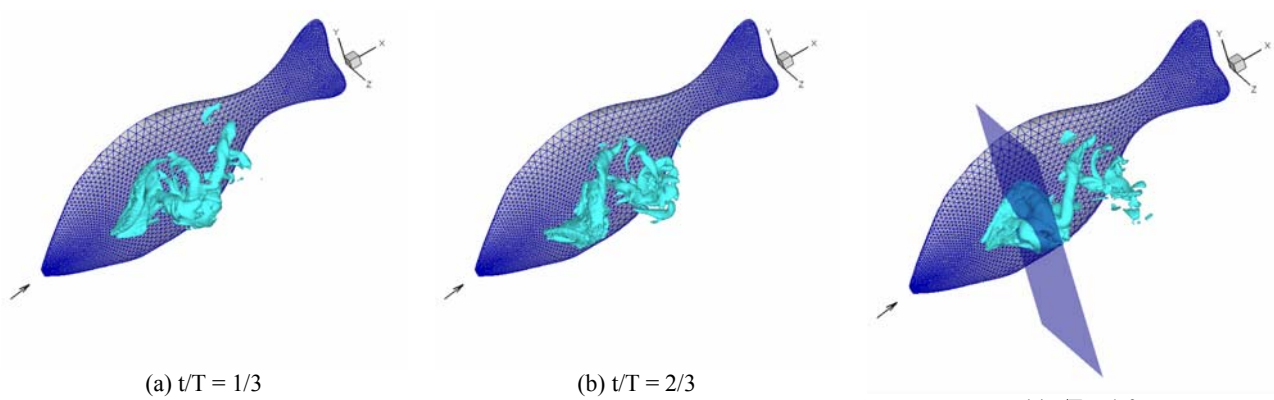

(a) t/T = 1/3 (b) t/T = 2/3 (c) t/T = 1.0

Figure 17. Enstrophy contours from CFD calculations at three different times during the fin beat based on actual sunfish fin kinematics.

One key quantity that the CFD simulations can provide is the hydrodynamic force that is produced by the fin. Figure 19 shows the coefficients corresponding to the three components of the force produced by the fin over one flapping cycle where the coefficient C_F for a given force F is computed as. $C_F = F/(1/2)\rho U_\infty^2 A_{fin}$ where A_{fin} is the nominal fin area. Figure 3(a) show the thrust coefficient and it is observed that not only are there two large peaks of thrust during the full cycle but that positive thrust is produced during all phases of the cycle. This behavior is very different from that observed for canonical rigid flapping foils where drag is usually produced at some phases in the cycle (*14, 15*) and hints at the superior thrust generation capability of this highly deformable fin. The mean thrust coefficient for this case is found to be 1.28. Figures 19(b) and (c) show the other two components of the forces produced by the fin and a number of interesting observations can be made regarding these plots. First, peak magnitudes of these transverse force components are smaller than

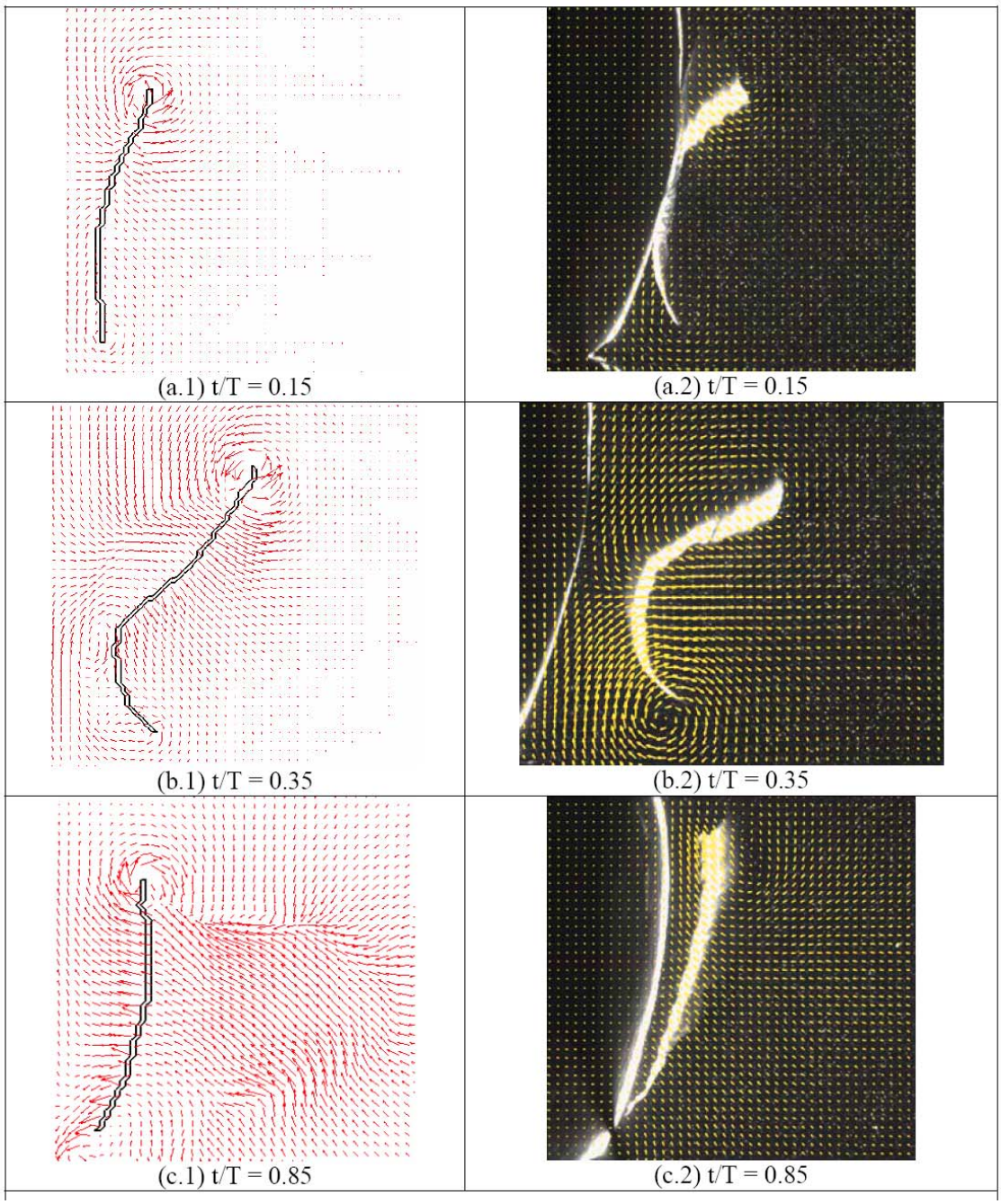

Figure 18. Vector plots on a streamwise plane located at 67% of from the root of the fin.

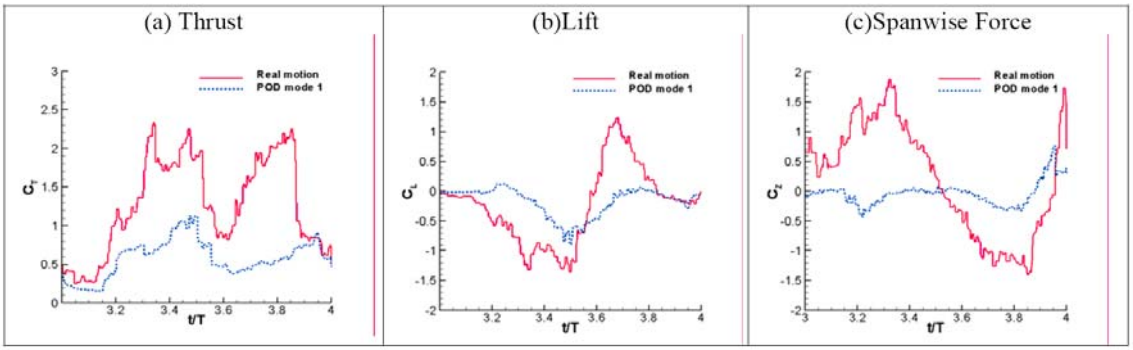

Figure 19. Computed temporal variation of thrust, lift, and spanwise force coefficients for the pectoral fin.

the peak thrust force. This is also highly unexpected since all existing data on rigid flapping foils (*14-17*) shows that the peak thrust force is significantly smaller than the lift and or spanwise force. This is clear indication of what we expect to be a relative high propulsive efficiency for this fin. Second, both these transverse forces have positive and negative variations in a cycle that of similar magnitudes. Consequently the mean values of these force components over one cycle are small, -0.19 for lift force and 0.12 for the spanwise force. These low mean values are not altogether unexpected since they allow the fish to minimize transverse body oscillations as it propels itself forward in a steady manner. Nevertheless, the fact that the current simulations are able to *predict* this behavior provides further proof of the fidelity of the extracted fin kinematics and the computational modeling approach.

Low-Dimensional Models of the Fin Pectoral Fin Kinematics and Associated Hydrodynamics

The kinematics of the pectoral fin and the resulting hydrodynamics is highly complex and does not lend itself easily to analysis based on simple notions of pitching/heaving/paddling kinematics or lift/drag based propulsive mechanisms. A more inventive approach is therefore needed which will allow us to dissect this highly complex motion and gain insight into the remarkable hydrodynamic performance of this pectoral fin. In the current study we employ proper orthogonal decomposition (POD) to extract the essential features of the fin gait and then employ CFD to examine the hydrodynamics of simplified gaits synthesized from the POD modes. POD is a powerful and elegant method for data analysis aimed at obtaining low-dimensional approximate descriptions of a high-dimensional process or dataset (*18*).

The POD method has been used in many disciplines including random variables, image processing, data compression and turbulent flow analysis, but our use of this technique for studying fish fins represents a first-of-its-kind effort.

In the POD analysis we employ 20 distinct time-frames that cover the full cycle of pectoral fin motion and the displacements taken by every node on the pectoral fin surface at each of these time-frames are inserted into a matrix. The matrix is then subjected to singular value decomposition (SVD) which then leads to 19 POD modes. The POD modes are then ranked in order of their corresponding singular values and allow us to easily determine the most energetic modes in the fish fin gait. The singular value spectrum for the fin is shown in Figure 20 along with a cumulative plot for the same data. The singular values are normalized by the sum of all the singular values whereas the cumulative values are rescales so that they sum to unity. A number of interesting observations can be made from this plot. First, the singular value spectrum shows three distinct ranges: the first between Mode-1 and 5 where we see a rapid decrease in the amplitude, the second from Mode-5 to 11 where there is a much slower reduction in amplitude and finally the range from Mode-12 to 19 which contains negligible energy.

The rapid initial decrease in the spectrum is interesting in that it suggests that a small number of

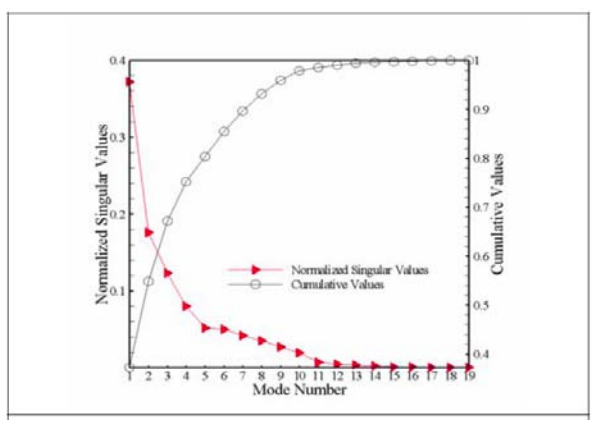

Figure 20. Normalized singular and cumulative values extracted from POD analysis of fin motion.

modes contain most of the essential features of the fin gait. In fact, the cumulative values show that the first two, three and five modes capture 55%, 67% and 80% respectively of the total motion. In the current study we are focusing on the first three modes because firstly they capture close to two-third of the total motion and secondly because each of these modes is highly distinct and relatively easy to interpret. Mode-1 is a "cupping" motion where the fin cups forward as it is abducted and leads to a rapid acceleration of the fin leading and trailing edges. Mode-2 is an "expansion" mode where the fin expands to present a larger surface area during adduction and finally Mode-3 involves a rapid "flick" of the spanwise tip of the fin.

In addition to providing insight into the fin kinematics, the POD analysis can be taken a step further by performing CFD simulations of fin gaits synthesized from the POD modes. This approach has the potential of allowing us to connect specific features in the fin gait to the observed vortex dynamics and hydrodynamics force production. The fin gaits have been synthesized by considering Mode-1, (Mode-1+Mode-2), (Mode-1+Mode-3) and (Mode-1+Mode-2+Mode-3). In the current paper, we present preliminary results from the Mode-1 simulations. The simulations are carried out on the same grid and at the same Reynolds and Strouhal numbers as the real fin. Figure 21 shows plots of the vortex topology for this low-dimensional fin gait and this plot can be compared directly with Figure 1 for the real fin motion. We observe that the tip vortices produced in this case are not as strong for the real fin motion. Furthermore, the Mode-1 simulation shows the formation of a distinct vortex ring in the fin wake which is not readily apparent for the fin when it undergoes the real motion.

A comparison of the hydrodynamic forces produced by the fin undergoing Mode-1 motion can also be made with the corresponding real motion (Fig. 19)). This comparison is quite illuminating. Even though Mode-1 based fin motion produces positive thrust during the entire cycle it does not produce nearly as much thrust as the real motion. In fact the mean thrust coefficient for this case is 0.58 which is only 45% of the thrust produced by the real fin. Interestingly, the second peak in thrust which occurs for the real fin during adduction is virtually eliminated in the Mode-1 motion case (Fig.19). This part of the thrust is likely associated with Mode-2 which is essentially activated during adduction and this hypothesis is currently being tested by performing the (Mode-1+Mode-2) simulation. Also interesting to note is the fact that the transverse forces are also significantly suppressed in the Mode-1 simulation. Thus, even though the thrust is lower in this case, it is possible that the propulsive efficiency has not deteriorated and this is another hypothesis that is currently being tested through a direct computation of the hydrodynamic efficiency of the fins.

VII. BIOMIMETIC FIN MODEL

A biomimetic, physical, robotic model of the bluegill sunfish pectoral fin has been developed that can reproduce many of the complex fin motions fish use for propulsion and maneuvering. The goal for this prototype was not to replicate either the anatomy or the complete functionality of the bluegill pectoral fish, but to develop a device capable of producing a broad array of motions that would be used to investigate which movements are fundamental to pectoral fin propulsion and control. By using a compliant mechanism based design, the biorobotic fin was able to produce a level of surface contouring and stiffness control sufficient to control the magnitude and direction of thrust. The prototype, which is constructed from traditional engineering materials and actuators, is also being used to define the architecture and functionality required by a biorobotic fin that will incorporate cofabricated conductive polymers as structural members, power delivery mechanism, and actuators.

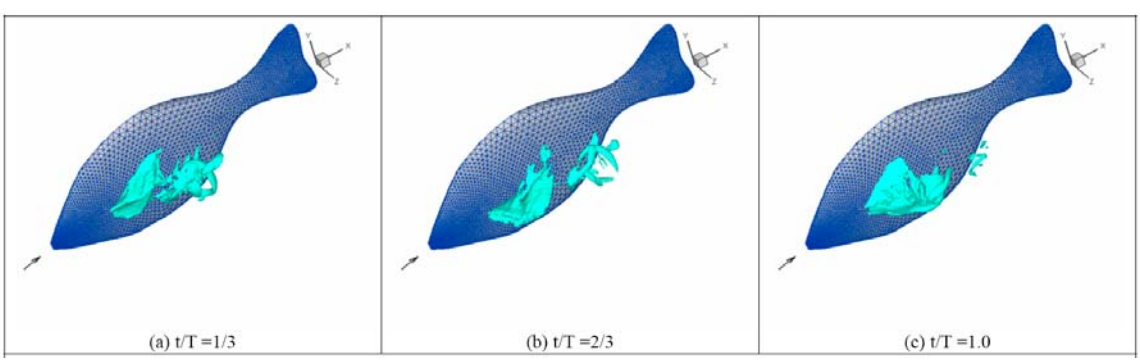

Figure 21. Enstrophy contours at three different times during the POD Mode-1 motion.

Three movements that affected the fin's surface and orientation were identified as the functional goals for the biorobotic model. These were: 1) spreading of the fin and surface area control, 2) curling of the distal ends of the fin rays towards their base, which is believed to control the stiffness of the fin's surface, and 3) sweep, or adduction and abduction, of the fin into and out of the flow. By controlling and combining these modes of motion, it was believed that the robotic fin would be capable of performing the steady swimming stroke as well as the strong and weak side evasive maneuvers.

The architecture of the biorobotic fin was based upon the anatomy of the sunfish fin; however several simplifications were made to simplify its manufacture and to reduce the complexity of its control. Three significant deviations from nature were: 1) reducing the number of fin rays per fin from fourteen to four, 2) reducing the number of actuators per fin ray from four to two, and, 3) eliminating the bifurcation and bony segmentation of fin ray. Bifurcation and segmentation are believed to be associated with the passive stiffness of the fin ray, which was addressed in the design by varying the cross-section of the fin ray and the material properties of the webbing.

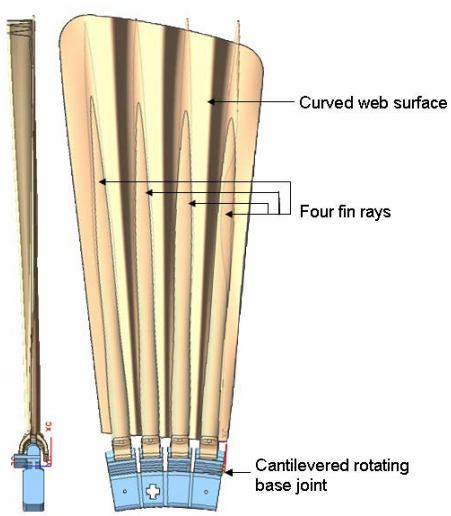

Figure 22. A CAD model of the fin designed using Unigraphix NX2. This illustrates notable features which include a curved web, four bilaminar rays, and a compliant base that provides a compliant hinge mechanism. Forces are applied through the fin ray base to actuate a spreading motion of the fin's surface area, the vertical shift at the base of the hemitrichia for bending the ray, as well as the rotational force for sweeping into and out of the flow.

The biorobotic fin, which is shown in Figure 22, was manufactured using rapid prototyping techniques. Molds and structural elements of the fin were printed using a 3D stereolithography printer with a resolution of 50×10^{-6} mm which allowed complex geometric features to be incorporated easily and quickly into the design. The web was cast in urethane with a durometer of 10 shore A and a tensile strength of 1.1 MPa. The base material is 60 shore A durometer urethane with a tensile strength of 3.5 MPa, and the fin rays were printed in an ultra-violet cured resin with a durometer of 85 shore D and a tensile strength of 65 MPa. High strength nylon tendons were used to attach to the fin rays to the base. The use of molding and casting techniques versus traditional assembly methods was done to help expedite an eventual transition from classical fabrication methods (e.g. using common materials and actuators) to co-fabrication (e.g. growing structural members, power delivery mechanisms, and actuators from a base set of elements).

The primary features of the structural design and the manner of actuating the fin are shown in Figure 22. The fin as it was modeled using Unigraphics NX-2 where the four bilaminar fin rays are embedded in a curved expandable web that rests on a compliant joint mechanism. The fin's span is expandable by a factor of two and the range of motion sweeping into the flow is close to 90 degrees. The tendons are attached at eccentrically located positions creating a moment about the center line of the ray; causing the fin to spread open increasing its surface area. Two holes are stacked vertically at the ray's base and are used to apply a vertical displacement between the two ends of the ray. This relative offset is required to achieve bending and is performed with a single actuator. The sweeping motion of the fin is achieved via tendon attachments

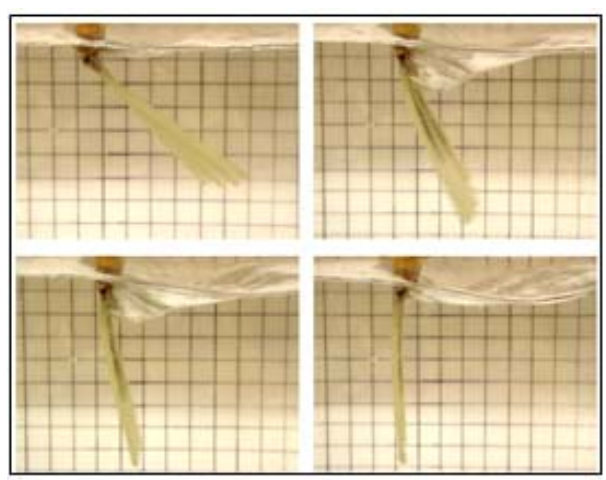

Figure 23. The fin was actuated to perform steady swimming in a flow of 0.55 $TL \cdot s^{-1}$ at 1 Hz. The model is being moved against the flow tank current and water surface deformation can be seen downstream of the fin.

and is generally the same tendon used to achieve the spreading motion. In this configuration the fin sweeps forward simultaneously as the surface area increases. The tendons are driven by pulse width controlled servo motors with an operating speed of 300 degrees per second at no load and a stall torque of 0.96 Kg·m.

The ability of the biorobotic fin to produce maneuvering and steady swimming maneuvers was tested in flows of up to 0.55 $TL \cdot s^{-1}$. The trajectories for the fin rays were derived from the kinematic data taken of the bluegill sunfish. Only the results of the steady and strong side swimming maneuvers are presented here.

Steady swimming locomotion is shown in Figure 23. For these movements, all of the fin rays were actuated in sweep and curl with equal amplitude and zero phase difference. Half of the complete stroke is shown in the freeze frames of Figure 23. In this test, the flow was set to a speed of 0.55 $TL \cdot s^{-1}$ and the fin rays were actuated at a frequency of 1 Hz. This was the fastest speed implemented in the flow tank. The large cone of water which is drawn from the surface by the fin clearly shows that this robotic design was capable of producing significant levels of thrust in a steady swimming mode.

The importance of the bilaminar fin ray design was verified when swimming was implemented with and without the curl motion during a steady swimming maneuver. There is no vortex shedding apparent without fin ray curling: a double set of vortices was shed one off each edge of the fin. This flow pattern is characteristic of the particle image velocimetry data taken from the bluegill sunfish during steady swimming, which shows the importance of active curl on performance.

This first biorobotic fin model has successfully demonstrated that a simplified fin model can produce generalized fin motions and hydrodynamics that mimic fish performing steady swimming and strong side maneuvers. It is an important first step towards developing AUVs that have the maneuverability and propulsion characteristics of fish.

It is clear that further progress can be made in terms of the articulation and power output of the fins. To address this, our next iteration of the biorobotic fin will: 1) explore increased variability of the stiffness of the fin over its length, 2) add two actuators in order to create a cupping motion of the fin, which may be critical for generating thrust in the abduction phase of the sweep stroke, and to decouple the spreading and sweeping actions of the fin, 3) incorporate a fifth fin ray in order to achieve a center line about which this cupping motion can be actuated, and 4) use linear Lorentz-force actuators whose functional behavior is more similar to muscles and conducting polymer actuators than servomotors. Ultimately, conducting polymers will be incorporated into the robotic model. Conducting polymers possess numerous desirable physical and active properties that make it possible to grow rather than build artificial muscles for an articulated device. Their potential for co-fabrication enables engineers to implement simpler more integrated devices as these materials have been shown to provide all the basic functional requirements of a biomimetic robot including: force sensors (analogous to the Golgi organs in tendons), strain sensors (like muscle spindles), structural elements (such as bones, joints, and webbing), and actuators (akin to muscle).

VIII. CONCLUSIONS AND PROSPECTUS

We have undertaken a multidisciplinary approach to understanding the function of fish pectoral fins with the aim of learning the basic principles of fin function and applying these to the construction of a biomimetic fish fin propulsor for AUVs. Fish fins are flexible and provide high maneuverability. A number of novel and previously unsuspected functional features of fish fins have been discovered and yet much remains to be learned. In particular the specific propulsive and maneuvering advantages of flexibility *per se* have yet to be uncovered, although our data provide several suggestions as to the significance of a flexible design. Design of a robotic fish-fin like propulsor could take advantage of many of the biological design features that have resulted from nearly 500 million years of selection for aquatic propulsive efficiency.

This research is supported by a MURI grant from the Office of Naval Research.

IX. REFERENCES

1. B. C. Jayne, A. Lozada, G. V. Lauder, *J. Morphol.* **228**, 307 (1996).
2. E. G. Drucker, G. V. Lauder, *J. Exp. Biol.* **202**, 2393 (1999).
3. E. G. Drucker, G. V. Lauder, *J. Exp. Biol.* **203**, 2379 (2000).
4. E. G. Drucker, G. V. Lauder, *J. Exp. Biol.* **204**, 431 (2001).
5. E. G. Drucker, G. V. Lauder, *J. Exp. Biol.* **204**, 2943 (2001).
6. A. Gibb, B. C. Jayne, G. V. Lauder, *J. Exp. Biol.* **189**, 133 (1994).
7. G. V. Lauder, in *The Physiology of Fishes, Third Edition* D. H. Evans, J. B. Claiborne, Eds. (CRC Press, Boca Raton, 2005) pp. in press.

8. G. V. Lauder, E. G. Drucker, J. Nauen, C. D. Wilga, in *Vertebrate Biomechanics and Evolution* V. Bels, J.-P. Gasc, A. Casinos, Eds. (Bios Scientific Publishers, Oxford, 2003) pp. 117-135.
9. G. V. Lauder, J. Nauen, E. G. Drucker, *Int. Comp. Biol.* **42**, 1009 (2002).
10. E. G. Drucker, G. V. Lauder, *J. Exp. Biol.* **206**, 813 (2003).
11. C. Brücker, *J. Fluid Struct.* **15**, 543 (2001).
12. R. Mittal, G. Iaccarino, *Ann. Rev. Fluid Mech.* **37**, 239–261 (2005).
13. M. Bozkurttas, D. H., S. V., M. R., N. F., *AIAA* **Reno, NV,**, 2005 (2005).
14. M. S. Triantafyllou, A. H. Techet, F. S. Hover, *IEEE J. Oceanic Eng.* **29**, 585 (2004).
15. R. Mittal, *IEEE J. Oceanic Eng.* **29**, 595 (2004).
16. G. C. Lewin, H. Haj-Hariri, *J. Fluid Mech.* **492**, 339 (2003).
17. K. Isogai, Y. Shinmoto, Y. Watanabe, *AIAA J.* **37**, 1145 (1999).
18. Y. C. Liang *et al.*, *J. of Sound and Vibration* **252**, 527 (2002).